Composite Structures 354 (2025) 118783

Contents lists available at ScienceDirect

Composite Structures

journal homepage: www.elsevier.com/locate/compstruct

Theoretical model combined finite element approach for studying mechanical behavior of shape memory hydrogel ribbed sheet with stretch-trigged bend effect

Yunqiang Hu [a], Chengjun Zeng [a], Jian Sun [b], Fei Jia [a,*], Jinsong Leng [b], Yanju Liu [a,*]

[a] Department of Astronautical Science and Mechanics, Harbin Institute of Technology (HIT), P.O. Box 301, No. 92 West Dazhi Street, Harbin 150001, People's Republic of China

[b] Center for Composite Materials and Structures, Science Park of Harbin Institute of Technology (HIT), P.O. Box 3011, No. 2 YiKuang Street, Harbin 150080, People's Republic of China

ARTICLE INFO

Keywords:
Shape memory hydrogel
Ribbed sheet
Stretch-trigged bend
Curvature-strain relationship

ABSTRACT

Shape memory hydrogels(SMHs) are a kind of novel shape memory soft materials. Although SMHs constitutive models have been developed, explorations about deformation laws of SMH structures are inadequate. As a kind of representative structure, a SMH ribbed sheet can deform to a circle due to stretch-trigged bend effect and its deformed configuration can be fixed due to shape memory effect. To date, deformation laws of SMH ribbed sheet are still unclear, which is not conducive to SMHs application. In this work, the mechanical behavior of SMH ribbed sheet is investigated through theoretical analysis and finite element simulation. The curvature-strain relationship is deduced for multi-materials and trapezium rib ribbed sheets. Then we demonstrated constraint swelling, uniaxial tension, and shape memory cycle of SMH ribbed sheet through finite element simulation based on our previously established constitutive model. Theoretical predictions and simulation outputs are compared and they are in agreement with each other. This work clarifies the deformation laws of the SMH ribbed sheet and could give guidance for SMHs structure design.

1. Introduction

Structures based on soft materials are ubiquitous in both nature and life, such as convoluted brain [1], natural leaves [2], eukaryotic flagella [3], metamaterials [4,5], soft machines [6,7] and so on. Much effort has been devoted to study the performances of soft material structures under tension, compression, bend, and twist [8–11]. Thanks to the flexibility and stretchability of soft materials, it is easier for their structures to achieve two or more deformation modes at the same time, which will lead to plentiful functionality. Huang et al. [3] reported flagellated soft micromachines, where the configurations of flagellated can be helical, spiral and planar. Frenzel et al. [12] presented a kind of three-dimensional mechanical metamaterials with compression-trigged twist. Yu et al. [13] investigated the influence of anisotropic material properties on shape formation and transition in helical ribbons, where ribbons can bend and twist through changing rib angles. Xin el at. introduced a kind of pixel mechanical metamaterials, which can achieve tension-twist [14]. Under external stimuli, some sheet configurations can be transformed from 2D to 3D due to internal stress [15,16].

As a kind of coupled deformation mode, some studies focus on the stretch-trigged bend effect and elucidate its mechanical mechanisms. For membrane, stretch-trigged bend phenomenons may be observed in some cases. Membrane will bend due to transverse shrinking during tension and the bend configuration can vanish under excess stretching [17–20]. An annular membrane will bend due to the necking effect under tension when its two ends are fixed [21]. Contrary to common sense, localized bulging will occur in a stretched gel tube due to surface tension [22,23]. In addition to membrane, 3D soft structures can also achieve a stretch-trigged bend effect [24]. They found that a ribbed sheet will bend during tension and the curvature is linearly increasing with stretch strain.

The above discussions focus on conventional soft materials. Structures based on shape memory soft materials are attractive since in addition to retaining the characteristics of structures based on soft materials, they present shape programmability due to shape memory effect. Shape memory soft materials may comprise shape memory polymers(SMPs) and shape memory hydrogels(SMHs). Compared with SMPs, shape memory mechanisms of SMHs are more complex, such as

* Corresponding authors.
E-mail addresses: feijia@hit.edu.cn (F. Jia), yj_liu@hit.edu.cn (Y. Liu).

https://doi.org/10.1016/j.compstruct.2024.118783
Received 6 May 2024; Received in revised form 23 November 2024; Accepted 10 December 2024
Available online 17 December 2024

thermo-aqueous coupling shape memory behaviors [25]. Shape memory hydrogel is a newly fashionable kind of hydrogel with shape memory effect [26–30], which can fix temporary shape and recover into its initial shape through stimuli-sensitivity dynamic bonds [31,32]. Recently, the mechanisms and performances of SMHs were investigated from various perspectives due to their potential applications in drug release, soft actuator and biomedical functions [31,33–36]. Chen et al. synthesized a kind of SMH through a facile physical mixing method and this SMH is tough and has excellent shape memory properties [37]. Wang et al. studied the adhesion properties of the double gel layers with shape memory effect, which can achieve rapid shape deformation and recovery, and tough adhesion [38]. Yin et al. designed reinforced gradient hydrogel structures with a rapid water-triggered shape memory effect [39]. In addition, 3D or 4D printing technologies of SMHs are developed rapidly [40–42] and SMHs can be utilized to achieve information encryption [43]. These studies are involved in various SMHs structures. Combining any functional structures and shape memory effect, structures fabricated by SMHs can achieve predetermined configuration switching to implement plentiful functions.

Although many SMH material systems are synthesized, exploration of SMH deformation mechanism is still at the very beginning. Adopting the macroscopic method, Chen et al. and Xue et al. developed shape memory hydrogel constitutive models for temperature and water-triggered shape memory effect, respectively [44,45]. In our previous works, we developed a micro-macroscopic constitutive model based on the transient network theory and simulated uniaxial tension and bend behaviors of basic structures [25]. These existing constitutive models focus on SMHs material properties. Research about deformation laws of SMH ribbed sheets is very few. In this work, we investigated the stretch-trigged bend effect of SMH ribbed sheet and clarified its deformation mechanisms through theoretical analysis and finite element simulation. On the one hand, we proposed mechanical theories for multi-materials ribbed sheet and trapezium rib. On the other hand, we demonstrated uniaxial tension and shape memory cycle of SMH ribbed sheet through finite element simulation based on our proposed constitutive model [25]. These results develop the theory of SMHs structure and can provide useful guidance for SMH applications in the fields of biomedical and soft actuator.

The structure of this paper is as follows. Our SMH constitutive model is briefly reviewed in Section 2. Mechanical deformation laws of SMHs ribbed sheet are revealed in Section 3, where we focus on membrane bend configuration. Section 4 presents deformed law of rib shapes and how rib and membrane curvature are affected by each other. Section 5 is a summary.

2. Constitutive model

2.1. Constitutive model of double network shape memory hydrogels

Double network strategy that the network structure of hydrogels contains two networks, one is the permanent network and the other is the transient network, is often introduced to endow hydrogels with shape memory effect [40,46]. A micro-macroscopic constitutive model of shape memory hydrogels is developed by our group for double network SMHs and the model is verified through experimental measurements [25]. Herein, we briefly review our SMHs model. The deformation gradient $\mathbf{F}$ is introduced to track SMH deforming from the reference configuration to the current configuration. We assume that the network is incompressible and the volume change is denoted by J: $J = \det \mathbf{F}$. The left Cauchy Green deformation tensor is defined as $\mathbf{B} = \mathbf{F}\mathbf{F}^{\mathrm{T}}$. By defining the free energy of SMHs as the network stretch term and the mixture term and after some derivations, the Cauchy stress is obtained as

$$\begin{aligned}\breve{\boldsymbol{\sigma}} = {} & \frac{N_I\Omega}{JJ_0}\left(J_0^{2/3}\mathbf{B}-\mathbf{I}\right)+\frac{N_{II}\Omega}{J}\left(\boldsymbol{\varsigma}-\mathbf{I}\right) \\ & +\left[\ln\left(\frac{JJ_0-1}{JJ_0}\right)+\frac{1}{JJ_0}+\frac{\chi}{J^2J_0^2}-\frac{\mu}{k_bT}\right]\mathbf{I},\end{aligned} \tag{1}$$

where $\mathbf{I}$ represents the second order identity tensor, $\breve{\boldsymbol{\sigma}} = \boldsymbol{\sigma}/(k_bT/\Omega)$, k_b is the Boltzmann constant, χ denotes the Flory–Huggins interaction parameter, T is the absolute temperature, Ω represents the volume of a water molecule, μ is the chemical potential, N_I, N_{II} denote the cross-linked chain densities for the permanent network and the temporary network, respectively. J_0 is free swelling volume ratio before mechanical deformation. Since the meaning of the logarithmic function $\ln\left(\frac{J-1}{J}\right)$ at $J = 1$ is lacking, J_0 is introduced to ensure the feasibility of numerical calculations. In addition to this reason, from the view of experiment, synthetic SMHs already contain some water molecules and it is difficult to remove all of them. The first and third terms on the right-hand side of Eq. (1) represent the stress of single network hydrogels. The second term denotes the stress contribution of the temporary network and its deformation tensor is obtained from a theory of transient network [47], namely

$$\boldsymbol{\varsigma} = \mathbf{F}\left(\mathbf{C}^{-1}(T_0)e^{-\bar{k}_d(T-T_0)}+\bar{k}_d\int_{T_0}^{T}e^{-\bar{k}_d(T-\Lambda)}\mathbf{C}^{-1}(\Lambda)d\Lambda\right)\mathbf{F}^{\mathrm{T}}, \tag{2}$$

where $\bar{k}_d$ is the frequency factor for bond dissociation and T_0 denotes the initial temperature. This equation can capture temporary network structure evolution during the thermal–mechanical shape memory effect.

2.2. Free swelling of the cube

Finite element simulations of free swelling of a cube are carried out. The geometry sizes of the cube were 5 mm × 5 mm × 5 mm and 1000 C3D20R meshes were used to disperse SMH. Under the condition $\breve{\boldsymbol{\sigma}} = 0$, the chemical potential can be derived from Eq. (1) as

$$\begin{aligned}\bar{\mu} = {} & \frac{N_I\Omega}{JJ_0}\left(J_0^{2/3}J^{2/3}-1\right)+\frac{N_{II}\Omega}{J}\left(J^{2/3}-1\right) \\ & +\ln\left(\frac{JJ_0-1}{JJ_0}\right)+\frac{1}{JJ_0}+\frac{\chi}{J^2J_0^2},\end{aligned} \tag{3}$$

where $\bar{\mu} = \mu/k_bT$. The chain density of the temporary network N_{II} as a function of temperature and N_I is defined as

$$N_{II} = f(T)R_EN_I, \tag{4}$$

where R_E is the total modulus ratio between the permanent and temporary networks, we took R_E = 10,100 and 1000, respectively. The temperatures adopted in this simulation are 283 K and 343 K, and the function $f(T)$ reflects the normalized cross-linking density of the temporary network and herein its values are assumed as $f(283\,\mathrm{K}) = 0$ and $f(343\,\mathrm{K}) = 1$, respectively, which conforms to experiment observations of the Acrylamide(AAm)-Methylcellulose(MC) hydrogel where the temporary network does not cross-link at 283 K and almost completely aggregated at 343 K [25,28]. In this free swelling process, the free chains cross-link to form the temporary network before the deformation process, and then $\boldsymbol{\varsigma} = \mathbf{B}$. We assume that volume expansion is homogeneous, then the form of the chemical potential does not affect the results and we chose $\bar{\mu} = \bar{\mu}_0\exp(-t/100.0)$. One static-general step was created and t is the step time. The chemical potential was introduced into all elements and all mechanical freedoms of one vertex of the cube were constrained. The parameters utilized in these simulations were $J_0 = 1.03$, $N_I\Omega = 0.001$, $\chi = 0.3$, and $\bar{\mu}_0 = -2.28244$.

To validate the finite element simulation, the theoretical results from Eq. (3) are also presented. Fig. 1 shows the results from FE simulation and theory, they agree with each other. The volume of SMHs expands with the ranging of the chemical potential for all R_E. The shear modulus affects the swelling process, namely, J decreases with R_E.

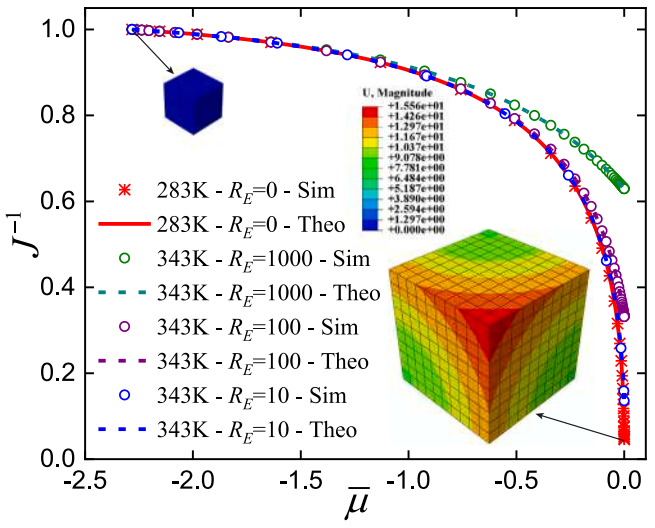

Fig. 1. Theoretical results and simulation outputs of SMHs at various modulus ratios during free swelling ($f(283\,\mathrm{K}) = 0$ and $f(343\,\mathrm{K}) = 1$).

3. Mechanics of the ribbed sheet

3.1. Stretch-triggered bend effect

In this section, we carry out uniaxial tension performances of SMHs ribbed sheet through theoretical analysis and finite element simulation. The main deformation feature of the ribbed sheet illustrated in Fig. 2(a) is stretch-triggered bend [24]. The effect law of the geometry size and material properties on deformed configuration is clarified. Figs. 2(b) and 2(c) present schematics of the angle and height of rib variation, respectively. We can obtain $\left(R-\Delta_y\right)^2+\Delta_z^2=R^2$ from the geometric relationship of the ribbed sheet illustrated in Fig. 2(d), where R denotes the sheet radius and Δ_y, Δ_z are location distances along Y, Z directions, respectively. Then the curvature is derived as

$$\kappa=\frac{1}{R}=\frac{2\Delta_y}{\Delta_y^2+\Delta_z^2}. \tag{5}$$

Considering a representative unit and following the theory of [24] under $\theta = 0$ and $H_2 = H_1$, the deformations of the membrane and the rib are

$$\begin{aligned}&\varepsilon_{xx}=\varepsilon, \sigma_{yy}=0, \varepsilon_{zz}=\kappa y+\varepsilon_M,\\ &\varepsilon_{xx}=0, \sigma_{yy}=0, \varepsilon_{zz}=\kappa y+\varepsilon_M,\end{aligned} \tag{6}$$

respectively, where ε denotes the uniaxial tension strain and ε_M represents the mid-plane strain of the membrane. Considering the Hookes constitutive model and ignoring the shear strains, the strain energy as a function of strain components is written as

$$\upsilon=\frac{E}{2(1+\nu)}\left[\frac{\nu}{1-2\nu}\left(\varepsilon_{xx}+\varepsilon_{yy}+\varepsilon_{zz}\right)^2+\varepsilon_{xx}^2+\varepsilon_{yy}^2+\varepsilon_{zz}^2\right], \tag{7}$$

where E, ν are the elastic modulus and the Poisson's ratio, respectively. We consider a general case that a ribbed sheet is composed of two materials, namely the membrane is shape memory hydrogel and the rib is rubbery. According to Eq. (1), shape memory hydrogels can be treated as Hookean materials with water molecule permeation. Combining the first line of Eq. (6) and (7), the elastic energy W_m stored in the representative unit membrane is deduced as

$$\begin{aligned}W_m=&\iiint \upsilon_m dV=\frac{1}{2}\frac{E_m\left(L_H+L_S\right)B}{\left(1-\nu_m^2\right)}\\ &\times\left[H^3\frac{\kappa^2}{12}+H\left(\varepsilon^2+2\nu_m\varepsilon_M\varepsilon+\varepsilon_M^2\right)\right],\end{aligned} \tag{8}$$

Table 1
Geometrical parameters in basic finite element simulation.

L	B	H	H_1	H_2	L_H	L_S	θ
1.8 mm	8 mm	0.4 mm	0.6 mm	0.6 mm	0.3 mm	0.3 mm	0

Table 2
Constitutive model parameters in basic finite element simulation.

$N_I\Omega$	$N_{II}\Omega$	J_0	χ	$\bar{\mu}$	T_0	$\bar{k}_d$
0.001	0.0	2.0	0.3	−0.118	283 K	0.0001 K^{-1}

where subscript m denotes the membrane. The elastic energy W_r stored in the unit representative rib is likewise written as

$$W_r=\iiint \upsilon_r dV=\frac{1}{2}\frac{E_r L_S B}{\left(1-\nu_r^2\right)}\left[H_1^3\frac{\kappa^2}{12}+H_1\left(\varepsilon_M+\kappa\frac{H_1+H}{2}\right)^2\right], \tag{9}$$

where m denotes the rib. As ε is fixed, the curvature κ can be obtained by minimizing the total elastic energy $W_{total} = W_m + W_r$ with respect to κ and ε_M, namely

$$\kappa=\frac{6H\phi H_1\left(H_1+H\right)}{\psi^{-1}H^4+4\phi H_1H^3+6\phi H_1^2H^2+4\phi H_1^3H+\psi\phi^2H_1^4}\nu\varepsilon, \tag{10}$$

where $\phi = L_S/(L_H + L_S)$ and $\psi = E_r/E_m$. Both shape memory hydrogel and rubbery are considered incompressible, so we have $\nu_m = \nu_r = \nu$. According to Eq. (10), the curvature is linearly increasing with uniaxial tension strain even if the rib and sheet are of two types of materials. When $\psi = 1$, which means that the membrane and rib are the same materials or two different materials with the same mechanical properties, Eq. (10) is simplified as the result of [24]

$$\kappa=\frac{6H\phi H_1\left(H_1+H\right)}{H^4+4\phi H_1H^3+6\phi H_1^2H^2+4\phi H_1^3H+\phi^2H_1^4}\nu\varepsilon. \tag{11}$$

We demonstrate FE simulation of SMHs ribbed sheet under uniaxial tension. Effects of main geometry and material parameters on ribbed sheet configuration are clarified, and FE results are compared with Eq. (10). We first simulate a basic example and then carry out parameter studies. SMH ribbed sheet is a periodic structure composed of membrane and rib and herein the number of periodic structures is three. Geometry parameters and constitutive model parameters utilized in the basic FE model are listed in Tables 1 and 2, respectively. In addition, in this basic FE example, we take both membrane and rib are SMHs, consequently $\psi = 1$.

Three representative units were chosen and only half of the model was created due to geometric symmetry along the Z-direction. X-direction degree of the left end was fixed, the right end was stretched along X direction, the chemical potential of all locations of ribbed sheet was $\bar{\mu}$ and the temperature was 283 K. 5040 C3D20R elements were used for discretizing the ribbed sheet. Fig. 3 illustrates snapshots of SMH ribbed sheet during stretch. The ribbed sheet bends during stretch and the curvature increases with uniaxial tension strain. The deformed configurations of membrane along the X-direction are almost the same due to boundary conditions, which means that three representative units are enough to capture SMH ribbed sheet deformation feature.

Fig. 4(a) shows configurations of the cross-section perpendicular to the stretching direction. The configurations with different tension strains are close to circumference. Fig. 4(b) compares the curvature-tension strain curves from Eq. (10) and FE simulation. Both theory results and simulation results show that κ linearly increases with ε even at large scale deformation. The simulation result is in agreement with the theory prediction. We then look into the effect of rib height on the relationship between strain and curvature. The values of H_1 are 0.1, 0.3, 0.6, 1.0, 1.5, 2.0, and 2.5, respectively and we make $H_2 = H_1$. Except for H_1 and H_2, other parameters are listed in Tables 1 and 2. In addition, also except for H_1 and H_2, geometry, mesh type and mechanical and chemical boundary conditions are following in

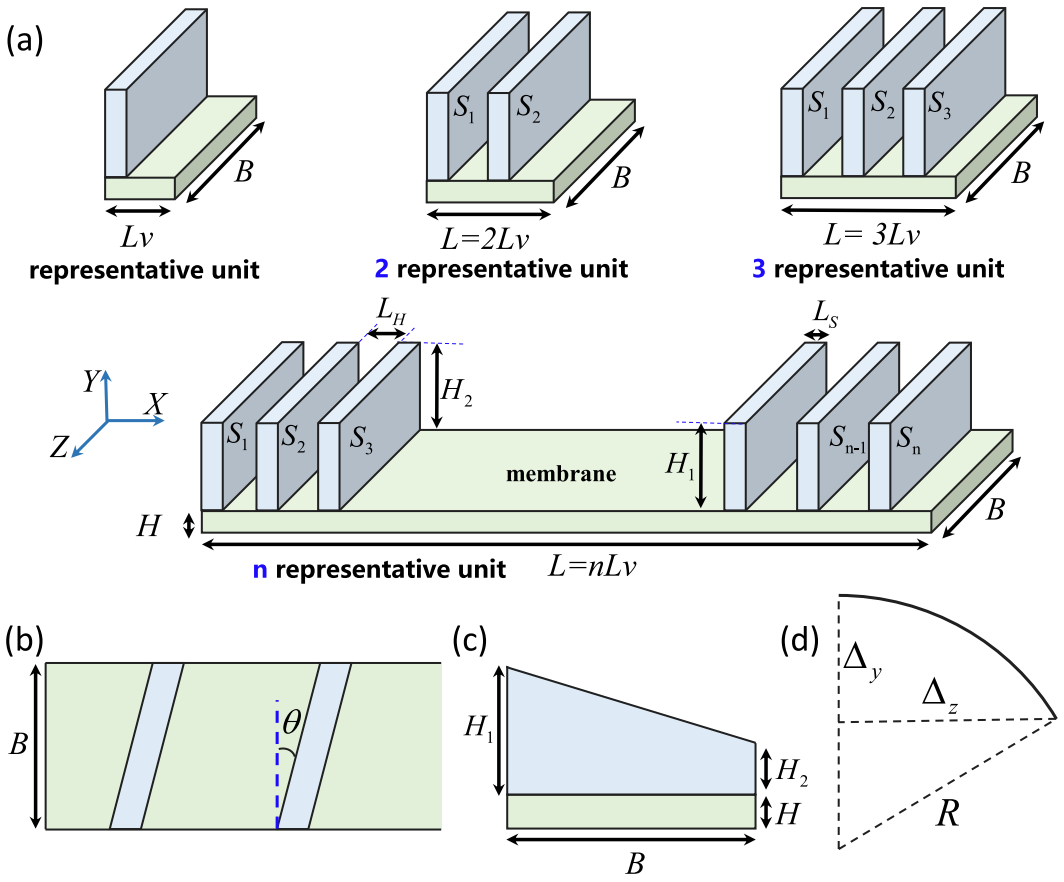

Fig. 2. Schematic diagram of shape memory hydrogel ribbed sheet: (a) geometry of SMHs ribbed sheet, representative unit consisted of membrane and a rib, 2, 3, n representative unit, respectively, (b) vertical view of the rib angle variation, (c) side view of the height of the rib, and (d) the curvature schematic diagram of the ribbed sheet.

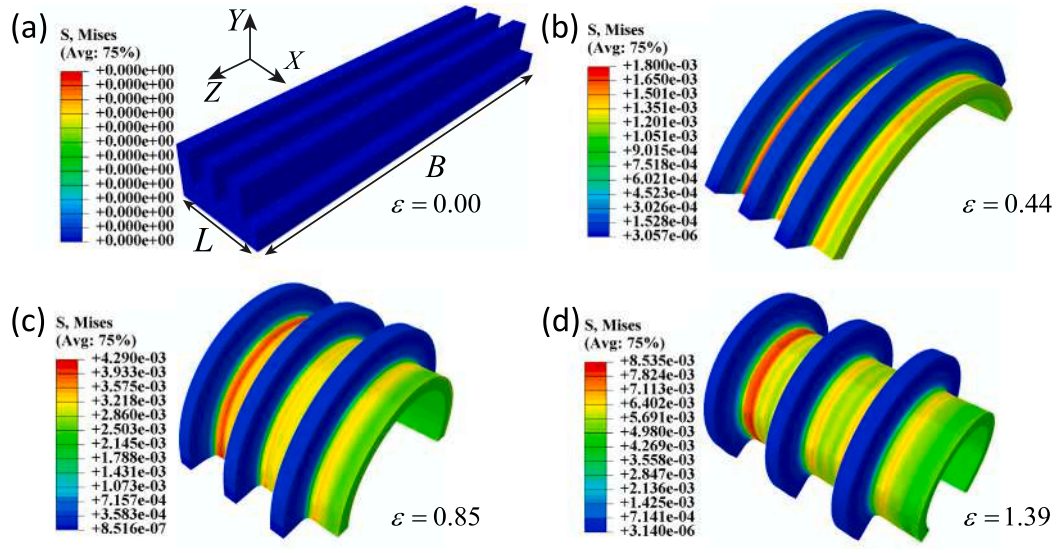

Fig. 3. Snapshots of SMHs ribbed sheet during stretch with various strains: (a) $\varepsilon = 0$, (b) $\varepsilon = 0.44$, (c) $\varepsilon = 0.85$, and (d) $\varepsilon = 1.39$.

the basic FE simulation. Fig. 4(c) shows half of the configurations of the ribbed sheet at $\varepsilon = 0.5$. The rib height has strong effects on the curvature under identical strain. Fig. 4(d) shows quantitative results of κ-H_1 from simulation and Eq. (10), which means that the relationship between curvature and rib height is not monotonic and κ first increases and then decreases with H_1.

We now investigate the stretch-trigged bend effect of the sheet with different rib angles: $\theta = 0°, 5°, 10°$ and $15°$. Asymmetric ribbed sheets are created and their geometrical sizes are 21 mm(L) × 8 mm(B) × 0.4 mm(H), the number of ribs is 30 and other parameters are the same as in Tables 1 and 2. All movement freedoms of the left end of the ribbed sheet are fixed. At the right end, except for moving along the X-direction displacement, all freedoms of movement are restricted. 34980 C3D20R elements are utilized to disperse the geometry. Fig. 5(a) shows the sheet snapshots and Fig. 5(b) illustrates the configuration curves of a single rib after stretch. For plotting simplicity, mid-points

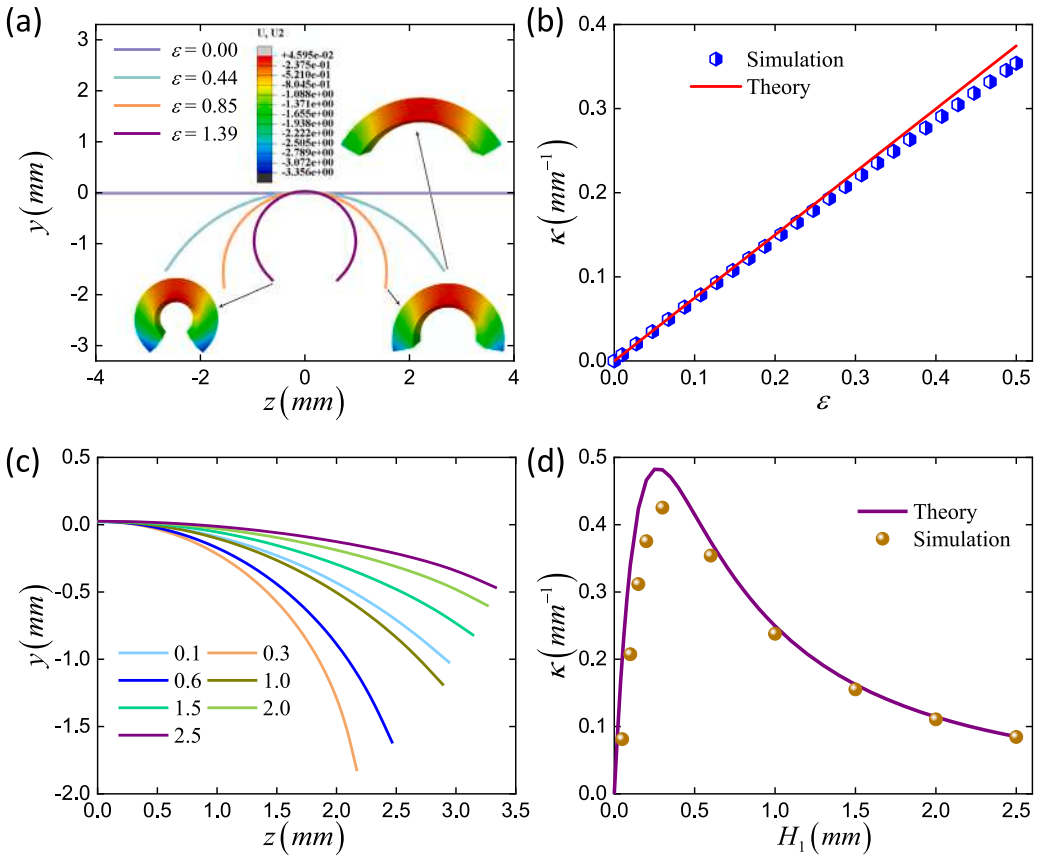

Fig. 4. Results of a sheet during stretch: (a) configurations of the sheet at different strains(finite element snapshots are added), (b) the curvature as a function of strain from theory and simulation, (c) half of configurations of the sheet with various H_1 at $\varepsilon = 0.5$, and (d) the curvature as a function of H_1.

of the configuration curves are moved to an identical point (0,0) and coordinates in X,Z-directions are denoted by $\bar{x}$ and $\bar{z}$, respectively. The displacement of the rib at 0° along X-direction is almost the same and then its current configuration is a straight line. Current configurations of rib are curves at $\theta = 5°$ and 10°. Interestingly, the configuration curve is also close to a straight line at $\theta = 15°$ but without paralleling that at $\theta = 0°$. The curvature of sheet as a function of the uniaxial tension strain can be obtained from simulation results, as illustrated in Fig. 5(c), which indicates that the curvature linearly increases with the strain at $\theta = 0°$, but linear law is not obeyed as the rib angle increases. These results match the law of [24].

The effect of rib slope on the stretch-trigged bend effect of sheet is also studied. SMH ribbed sheets are created and their geometrical sizes are 21 mm(L)×8 mm(B)×0.4 mm(H). The number of ribs is 30. The rib height on one side is fixed as $H_1 = 0.6$ mm, the heights on the other side are $H_2 = 0, 0.6, 1.5$ and 2.5 mm, respectively, and other parameters are the same as in Tables 1 and 2. The boundary conditions are the same as the SMH ribbed sheet investigating the rib angle depicted in Fig. 5(a). 54108 20-node quadratic brick, reduced integration elements are adopted. Configurations of sheet after stretch are shown in Fig. 6(a). It can be seen that the symmetry of the configuration is broken due to the slope of rib and the degree of asymmetry increases as H_2 is far away from H_1. Fig. 6(b) shows the curvature-strain curves during stretch. All curves show that a linear relationship is obeyed for four slopes. During stretching, the curvature of the two halves of the ribbed plate along the z-direction is different. The curvature does not monotonously increase as the slope, whether H_2 is greater than or less than H_1 resulting in the curvature decreasing than the value of case $H_1 = H_2$. From these results, we can conclude that the curved configuration of the ribbed sheet can be designed by changing the rib slope.

Above discussions are focused on one kind of material, namely $\psi = 1$. The sheet composed of multi-materials shows richer design parameters and may have more potential applications. Herein, we investigate the mechanical behaviors of ribbed sheets with various modulus ratios. The membrane is treated as shape memory hydrogels and its constitutive model is listed in Eq. (1). The rib is considered the incompressible neo-Hooken material and its free energy density and the Cauchy stress are

$$W = C_{10}\left(F_{ij}F_{ij} - 3\right), \text{and}$$
$$\boldsymbol{\sigma} = 2C_{10}\mathbf{B} - p\mathbf{I}, \tag{12}$$

respectively, where C_{10} is the material parameter and p is introduced to match the incompressible condition.

Fig. 7(a) shows the effect of H_1 on κ with various modulus ratios ψ from Eq. (10). As H_1 increases, $\kappa/\upsilon\varepsilon$ first increases and then decreases for all modulus ratio ψ. However, the non-monotonic law can only be observed in a limit range. For example, within the horizontal coordinate range of Fig. 7(a), it can be found that $\kappa/\upsilon\varepsilon$ varies nonmonotonically with H_1 at $\psi = 50$ and $\kappa/\upsilon\varepsilon$ increases with H_1 at $\psi = 0.001$, which can be used to design κ-H_1 relationship through changing ψ. Fig. 7(b) shows the curves between ψ and $\kappa/\upsilon\varepsilon$. The effect law of ψ on κ is similar to the non-monotonic law between H_1 and κ. Consequently, we can conclude that for any H_1, there is a suitable ψ such that κ will reach a maximum value or for any ψ, there is a suitable H_1 such that κ will reach a maximum value.

We now carry out FE simulation of SMHs-rubbery ribbed sheet and we take ψ as 0.13, 0.63, 2.52 and 5.04, respectively. The boundary conditions, geometry and mesh type are the same as the basic FE simulation displayed in Fig. 3. The parameters of SMH constitutive model listed in Table 2 are also utilized. Fig. 7(c) illustrates the configurations of the ribbed sheet after stretch, which also shows that ψ strongly affects deformed shapes. Fig. 7(d) shows the curves between κ and ε from theory and FE simulation with various ψ. Theory predictions and FE outputs are in agreement with each other when ψ is close to

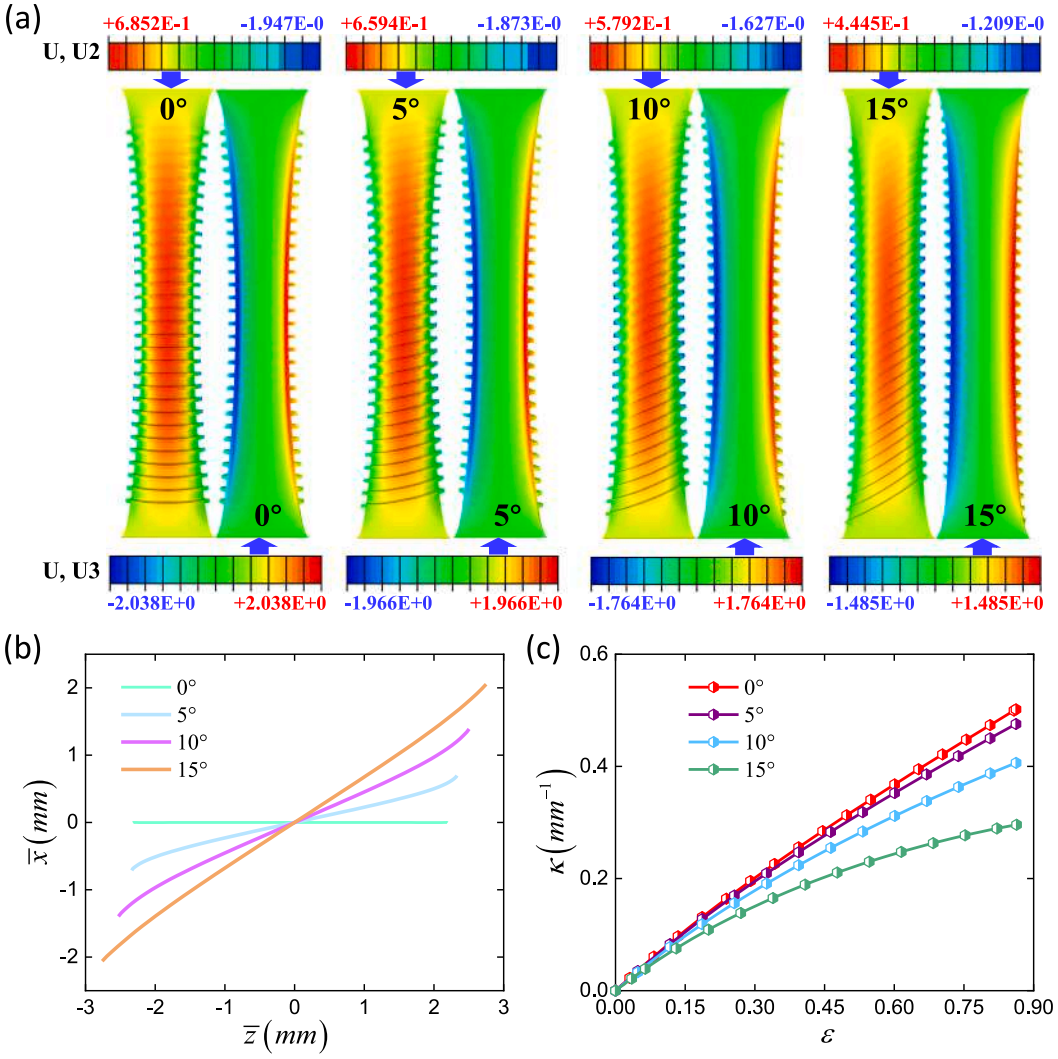

Fig. 5. Simulation results of the ribbed sheet with four rib angles: (a) snapshots of sheet after stretch, (b) configuration curves and (c) κ as a function of ε.

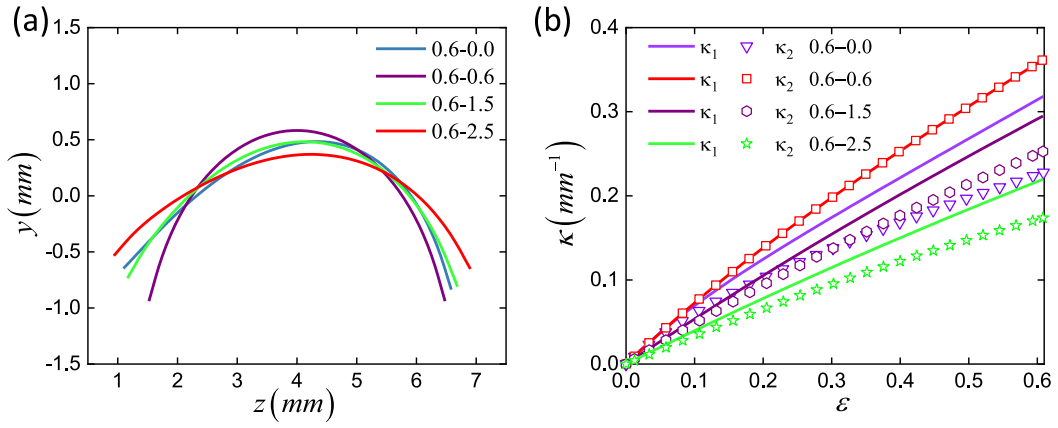

Fig. 6. FE simulations of the ribbed sheet with various rib slopes: (a) configurations after stretch and (b) curvature obtained from two halves of ribbed sheet along the Z-direction as a function of strain.

1. However, discrepancy exists as ψ stays away from 1, which may be caused by the hypothesis that ignoring some strain components. When $\psi < 1$, the rib is softer than the membrane and would be deformed along the X-direction, namely $\varepsilon_{xx} \neq 0$. This is different from Eq. (6) and may cause a discrepancy between theory and simulation. When $\psi > 1$, the rib is harder than the membrane. Both the rib and the membrane

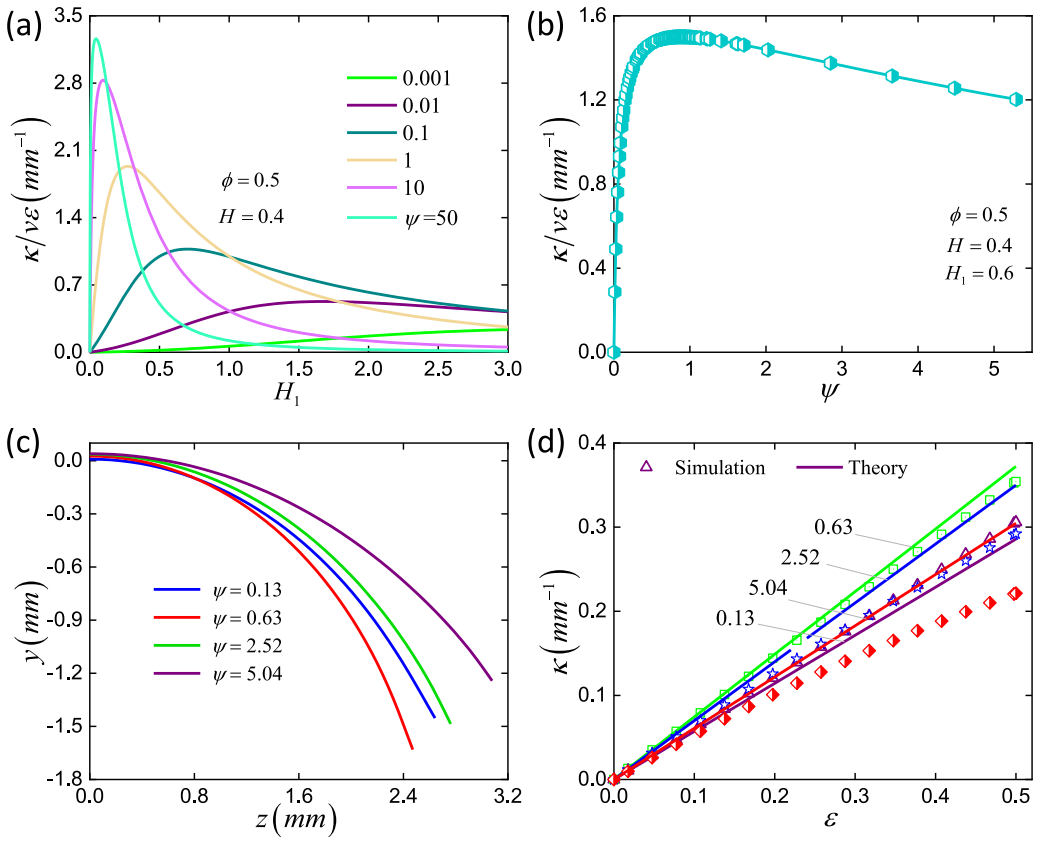

Fig. 7. Results of SMHs-rubbery ribbed sheet from theory Eq. (10) and FE simulation: (a) $\kappa/\upsilon\varepsilon$ as a function of H_1 with various ψ, (b) $\kappa/\upsilon\varepsilon$ as a function of ψ, (c) deformed shapes of the ribbed sheet after tension with various ψ, and (d) comparisons of curves between κ and ε from theory and simulation.

could be deformed along the Y-direction, namely $\varepsilon_{yy} \neq 0$, which may cause the resulting discrepancy.

3.2. Shape memory effect of the ribbed sheet

Combining the shape memory effect and stretch-trigged bend effect of the SMH ribbed sheet, a simple initial configuration can be transformed into a complex shape and then be fixed. Herein, we investigate the shape memory behaviors of SMHs ribbed sheet through FE simulation.

Similar to the basic simulation shown in Fig. 5, half of the model with three representative ribs was created and 5040 C3D20R elements were used. X-direction degree of the left end was fixed, the right end was stretched along the X-direction, and the chemical potential of the ribbed sheet was $\bar{\mu}$. Four steps were set up, corresponding to stretch at low temperature, maintaining displacement meanwhile heating, removing displacement constraint and cooling. Temperature varied between 283 K and 343 K and the amount of the right-end strain was 50%. In Eq. (4), the function $f(T)$ was defined as

$$f(T) = \frac{1}{1 + \exp\left(-\frac{T-\bar{T}}{\Delta}\right)}, \tag{13}$$

where $\bar{T} = 313K$ and $\Delta = 5K$. Fig. 8 illustrates the snapshots of SMHs at the end of each step, which shows that SMH ribbed sheet bend during stretch and bent configuration can be fixed. After a temperature cycle, the sheet can recover to its initial shape. To clarify the effect law of the modulus ratio of two networks, we take $R_E = 3, 10, 30$ and 50 in Eq. (4).

Fig. 9(a) shows the curves of $f(T)$ as a function of T with various R_E. In the first step, the chains of the transient network are not cross-linked, namely $f(T)$ is almost zero. In the second step, $f(T)$ increases due to heating and its amplitude is determined by R_E. $f(T)$ maintains a constant in the third step. In the last step, R_E closes 0 due to cooling-induced dynamic cross-linking broken. Fig. 9(b) shows the curvature-temperature curves during the shape memory cycle. The modulus ratio R_E affects shape fixed ratio and deformation curve. Both the shape fixed ratio at the end of step 3 and the curvature during step 4 increase with R_E. These results mean that the SMHs ribbed sheet performs stretch-trigged bend and the programmed shape can be maintained at various temperatures, which endows the ribbed sheet with plentiful design parameters.

4. Deformation law of the rib

In Section 3, we investigate the mechanics of shape memory hydrogel ribbed sheet through swelling, uniaxial tension with various geometry and material parameters, and shape memory cycle. We focus on the membrane deformation law in Section 3 and in this section, we reveal the rib deformation law. These discussions may give guidance for microscopic configuration fabrication.

4.1. Trapezium rib

As illustrated in Fig. 10, a representative volume unit section is composed of a membrane and a trapezium rib. The deformation law is explored through theory and FE simulation.

We consider that the strain conditions of the trapezium rib are the same as that of the rectangle rib. Combining Eqs. (6) and (7), the elastic

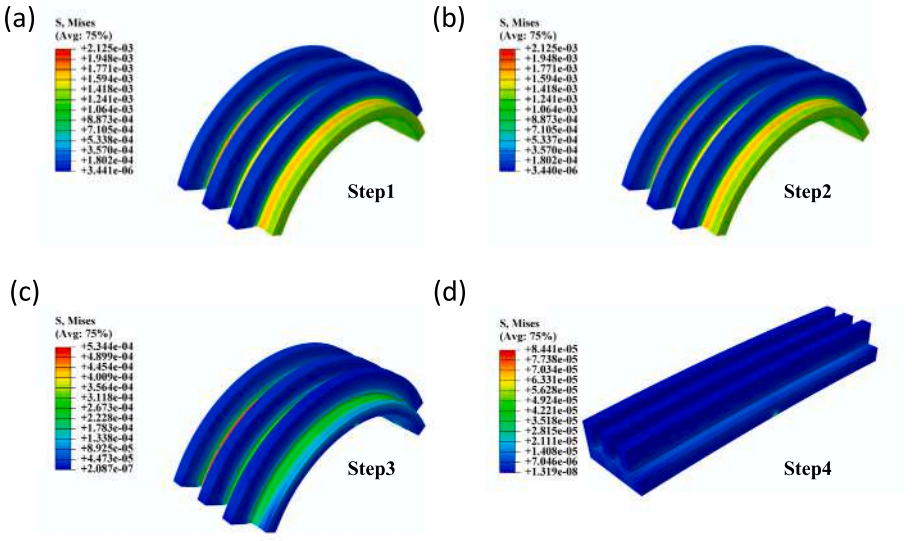

Fig. 8. Snapshots of SMHs ribbed sheet during shape memory cycle: (a)–(d) at the end of steps 1–4, respectively.

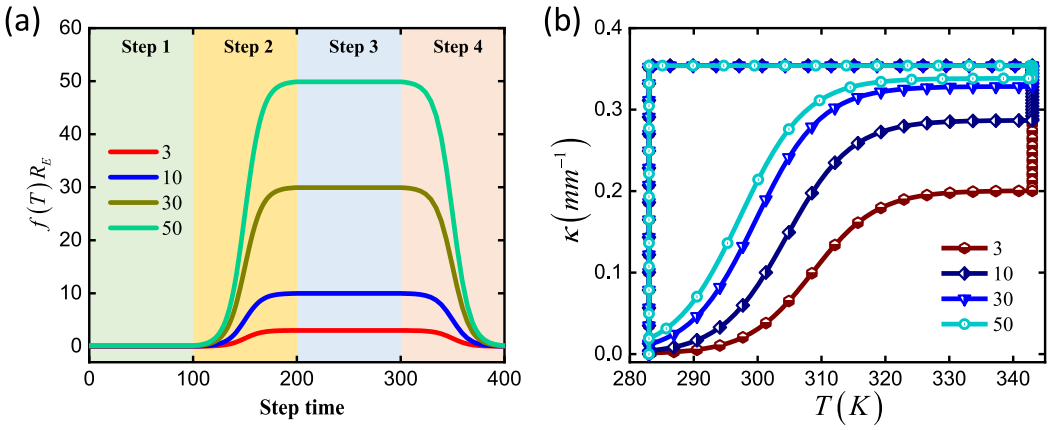

Fig. 9. Finite element simulation results of SMH ribbed sheet: (a) $f(T)$ as a function of step time with various R_E and (b) κ as a function of T.

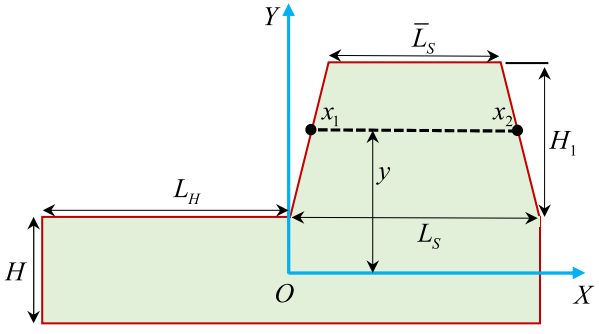

Fig. 10. Geometry of representative volume unit section of a trapezium ribbed sheet.

energy of trapezium rib is

$$W_r = \iiint \frac{E}{2(1-\nu^2)}\varepsilon_{zz}^2 dV = \frac{EB}{2(1-\nu^2)}\iint \varepsilon_{zz}^2 dS$$
$$= \frac{EB}{2(1-\nu^2)}\int_{H/2}^{H/2+H_1}\left(\int_{x_1(y)}^{x_2(y)} dx\right)\varepsilon_{zz}^2 dy \tag{14}$$
$$= \frac{EB}{2(1-\nu^2)}\int_{H/2}^{H/2+H_1}\varepsilon_{zz}^2\left(x_2(y)-x_1(y)\right)dy,$$

where

$$x_1(y) = \frac{L_S-\bar{L}_S}{2H_1}y - \frac{L_S-\bar{L}_S}{4H_1}H, \quad \text{and}$$
$$x_2(y) = -\frac{L_S-\bar{L}_S}{2H_1}y + \frac{L_S-\bar{L}_S}{4H_1}H + L_S. \tag{15}$$

Substituting Eqs. (6) and (15) into Eq. (14) and integrating, the expression of W_r is written as

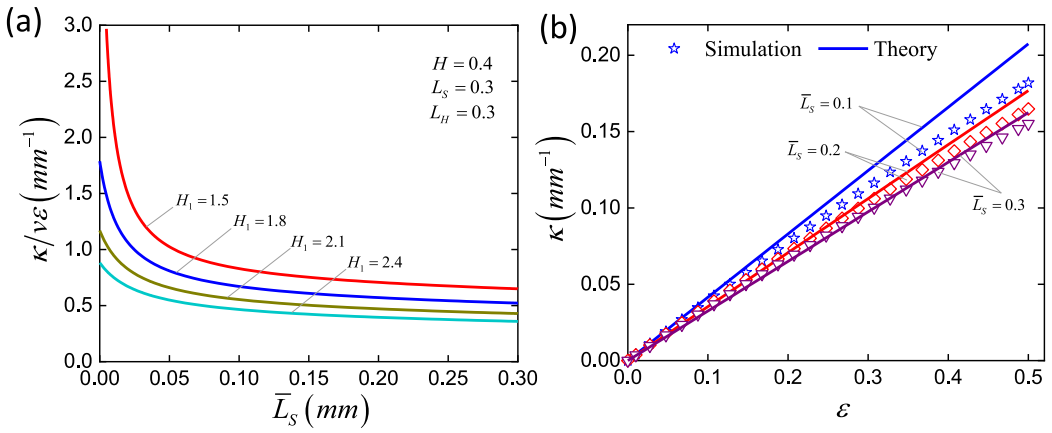

Fig. 11. Results of ribbed sheet with trapezium rib from theoretical predications and finite element simulation : (a)$\kappa/v\epsilon$ as a function of $\bar{L}_S$ from Eq. (17) and (b) comparisons of κ-ε curves from theoretical predictions and simulation outputs.

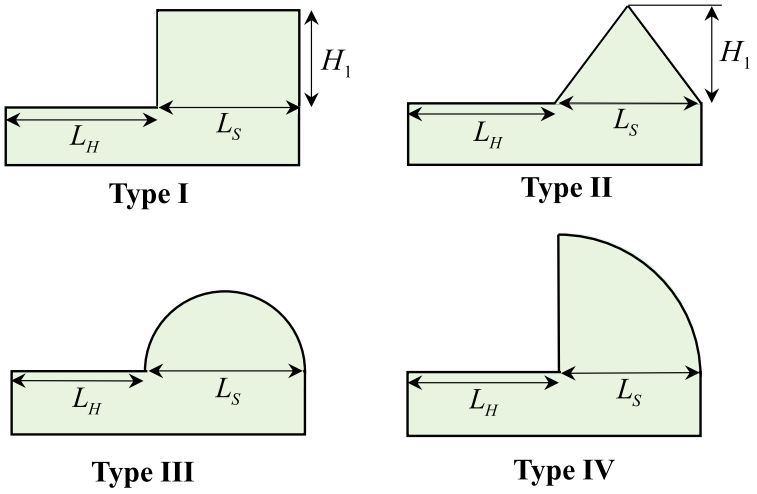

Fig. 12. Schematic geometry of four representative volume unit sections. Type-I is a rectangle, Type-II is a triangle, Type-III is a semicircle and Type-IV is a quadrant.

$$
\begin{aligned}
W_r =& \frac{E_r B L_S}{48\left(1-v_r^2\right)}\left[2H_1^3\kappa^2 - 4H_1^2\kappa\left(\kappa H - 2\varepsilon_M\right) - 6H\left(\kappa H + 2\varepsilon_M\right)^2\right.\\
&\left. - 3H_1\left(3\kappa^2H^2 + 4\kappa H\varepsilon_M - 4\varepsilon_M^2\right)\right]\\
&+\frac{E_r B \bar{L}_S}{48\left(1-v_r^2\right)}\left[6H_1^3\kappa^2 + 16H_1^2\kappa\left(\kappa H + \varepsilon_M\right) + 6H\left(\kappa H + 2\varepsilon_M\right)^2\right.\\
&\left. +3H_1\left(5\kappa^2H^2 + 12\kappa H\varepsilon_M + 4\varepsilon_M^2\right)\right].
\end{aligned}
\tag{16}
$$

Using Eqs. (8) and (16) and minimizing $W_m + W_r$, the curvature κ is obtained as

$$
\begin{aligned}
\kappa &= \frac{6\left[2\left(2\bar{L}_S + L_S\right)H_1^2 + 3\left(3\bar{L}_S - L_S\right)H_1 H + 6\left(\bar{L}_S - L_S\right)H^2\right]\left(L_H + L_S\right)H}{C_0 + C_1 H + C_2 H^2 + C_3 H^3 + C_4 H^4}v\epsilon,\\
C_0 &= \left(\bar{L}_S^2 + 4\bar{L}_S L_S + L_S^2\right)H_1^4,\\
C_1 &= \left(6\bar{L}_S^2 + 18\bar{L}_S L_H + 18\bar{L}_S L_S + 6L_H L_S\right)H_1^3,\\
C_2 &= \left(6\bar{L}_S^2 + 48\bar{L}_S L_H + 36\bar{L}_S L_S - 12L_H L_S - 6L_S^2\right)H_1^2,\\
C_3 &= \left(48\bar{L}_S L_H + 48\bar{L}_S L_S - 24L_H L_S - 24L_S^2\right)H_1,\\
C_4 &= 24\bar{L}_S L_H + 6L_H^2 + 24\bar{L}_S L_S - 12L_H L_S - 18L_S^2.
\end{aligned}
\tag{17}
$$

It can be found that Eq. (17) can be simplified as Eq. (10) when $\bar{L}_S = L_S$ and $\psi = 1$. Fig. 11(a) shows the curves of $\kappa/(v\epsilon)$ as a function of $\bar{L}_S$ with various of H_1. It can be found that $\kappa/(v\epsilon)$ decreases with $\bar{L}_S$.

FE simulations are demonstrated with various $\bar{L}_S = 0.1, 0.2, 0.3$ mm and material parameters are the same as the basic FE simulation. The ribbed sheet containing three ribs was created and 3720 C3D20R elements were adopted to disperse it. In this simulation, membrane sizes were 1.8 mm × 4 mm × 0.4 mm and we took H_1 = 1.5 mm, L_S = 0.3 mm and L_H = 0.3 mm. The displacement along the X-direction at the left end is restricted and that of the right end is stretched. Fig. 11(b) shows $\kappa - \varepsilon$ curves with various $\bar{L}_S$ from FE simulation and theory. They agree with each other. However, we found that the discrepancy will increase as $\bar{L}_S$ decreases, especially $\bar{L}_S$ is closed to 0, which may be caused by the difference in strain energy of rib caused by the hypothesis that the mid-surface of membrane is treated as XZ-plane.

4.2. Various ribs

In addition to stretch-trigged bend, the rib deformation law of the shape memory hydrogels ribbed sheet is engaging. During the shape memory cycle, regular rib shapes can be deformed to complex configurations and then be fixed by the shape memory effect. As shown in Fig. 12, four regular ribs are formulated, which are rectangle, triangle, semicircle and quadrant, respectively. In these FE simulations, parameters, mesh types, step and boundary conditions are the same as in Section 3.2.

Fig. 13(a)–(d) present snapshots of four ribbed sheets at the end of step1, which show that regular rib configurations have deformed into complex shapes. Fig. 14(a) illustrates ribbed sheet deformed snapshots of four type sections at the end of step 1 and Fig. 14(b) presents the κ-T relationship during the shape memory cycle. These results show the

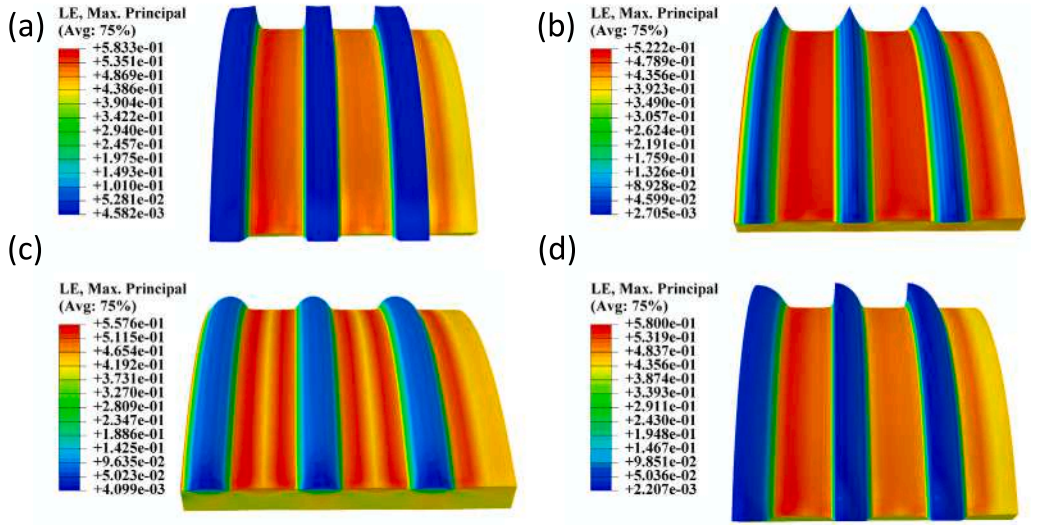

Fig. 13. Snapshots of the ribbed sheets at the end of step1: (a)–(d) are Type-I, II, II and IV, respectively.

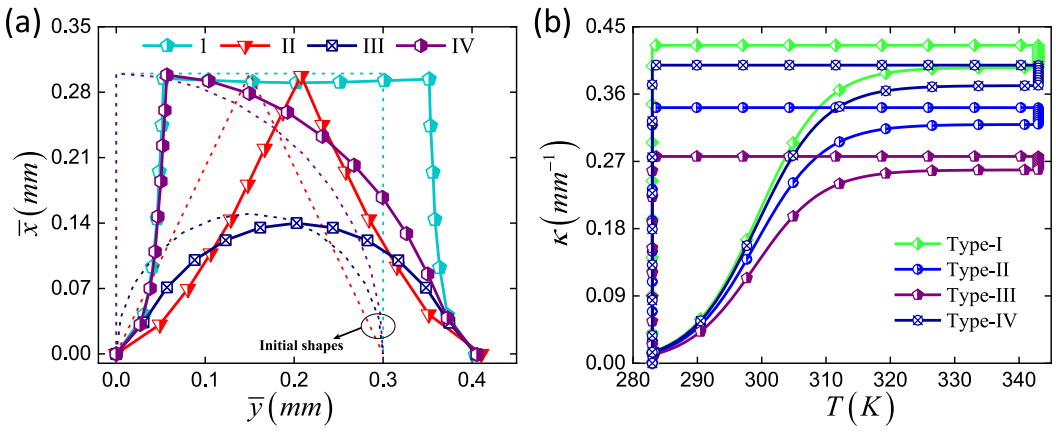

Fig. 14. (a) Section configurations of four type ribs. The left ends of all curves are moved to an identical point. In order to distinguish the current coordinates in ABAQUS, notations $\bar{x}$ and $\bar{y}$ are used. (b) κ-T relationship with various rib shapes during shape memory effect.

membranes bend due to stretching and the rib sections are evolving at the same time. The membrane curvature and rib configuration are affected by each other, which gives design freedoms for microshape fabrication.

5. Conclusions

In summary, through theoretical analysis and finite element simulation, we investigate the mechanical behaviors of shape memory hydrogel(SMH) ribbed sheet, which presents stretch-trigged bend effect and shape memory effect. The SMH ribbed sheet will bend under uniaxial tension and we derive the curvature-strain relationship for two materials, which shows that at the same strain, the curvature is non-monotonic changing with both rib height and modulus ratio of rib and membrane. The curvature-strain relationship for the trapezium rib is also obtained and the bend curvature decreases as the trapezium rib surface. Shape memory cycle simulations of SMH ribbed sheets indicate that ribbed sheets can fix temporary bent shape and recover its initial shape. In addition, the basic rib shapes, such as rectangle, triangle, semicircle and quadrant, can also be transformed into complex configurations and fixed by shape memory effect. We develop the theory of SMH basic structure and these results reveal the deformation law of SMH ribbed sheet, which provides a useful tool and guidance to design SMH complex functional structures.

CRediT authorship contribution statement

Yunqiang Hu: Writing – review & editing, Writing – original draft, Visualization, Formal analysis, Conceptualization. **Chengjun Zeng:** Writing – original draft, Visualization, Formal analysis, Conceptualization. **Jian Sun:** Writing – original draft, Formal analysis, Conceptualization. **Fei Jia:** Writing – review & editing, Writing – original draft, Visualization, Methodology, Formal analysis, Conceptualization. **Jinsong Leng:** Writing – original draft, Project administration. **Yanju Liu:** Writing – original draft, Supervision, Project administration, Methodology, Conceptualization.

Declaration of competing interest

The authors declare that they have no known competing financial interests or personal relationships that could have appeared to influence the work reported in this paper.

Acknowledgments

This work is supported by National Key R&D Program of China (2022YFB3805700).

Data availability

Data will be made available on request.

References

[1] Dai A, Ben Amar M. Minimizing the elastic energy of growing leaves by conformal mapping. Phys Rev Lett 2022;129:218101.
[2] Huang C, Wang Z, Quinn D, Suresh S, Hsia KJ. Differential growth and shape formation in plant organs. Proc Natl Acad Sci 2018;115(49):12359–64.
[3] Huang H, Sakar M, Petruska A, Pané S, Nelson B. Soft micromachines with programmable motility and morphology. Nature Commun 2016;7:12263. http://dx.doi.org/10.1038/ncomms12263.
[4] Bertoldi K, Vitelli V, Christensen J, Van Hecke M. Flexible mechanical metamaterials. Nat Rev Mater 2017;2(11):1–11.
[5] Chen Y, Ai B, Wong ZJ. Soft optical metamaterials. Nano Convergence 2020;7(1):18.
[6] Cacucciolo V, Shintake J, Kuwajima Y, Maeda S, Floreano D, Shea H. Stretchable pumps for soft machines. Nature 2019;572(7770):516–9.
[7] Liu X, Liu J, Lin S, Zhao X. Hydrogel machines. Mater Today 2020;36:102–24.
[8] Zhang P, Xu Z, Wu Z, Xu P, Yang C. Strengthening poly (2-hydroxyethyl methacrylate) hydrogels using biochars and hydrophobic aggregations. Int J Smart Nano Mater 2022;13(4):561–74.
[9] Liu Y, Chen Y, Zhu J, Lu M, Jiang C, Fan Z, Sun T. Time-dependent mechanical behavior of tough hydrogels under multiaxial stretching. Int J Smart Nano Mater 2023;14(4):460–73.
[10] Zhang S, Wei H, Tang J. Self-sensing magnetic actuators of bilayer hydrogels. Int J Smart Nano Mater 2023;14(4):496–509.
[11] Qiu Y, Ye H, Zhang S, Zhang H, Zheng Y. An explicit structural optimization method for temperature-sensitive hydrogel actuation devices. Compos Struct 2023;324:117521.
[12] Frenzel T, Kadic M, Wegener M. Three-dimensional mechanical metamaterials with a twist. Science 2017;358(6366):1072–4.
[13] Yu X, Zhang L, Hu N, Grover H, Huang S, Wang D, Chen Z. Shape formation of helical ribbons induced by material anisotropy. Appl Phys Lett 2017;110(9):091901.
[14] Xin X, Liu L, Liu Y, Leng J. 4D pixel mechanical metamaterials with programmable and reconfigurable properties. Adv Funct Mater 2022;32(6):2107795.
[15] Zhang Q, Wommer J, O'Rourke C, Teitelman J, Tang Y, Robison J, Lin G, Yin J. Origami and kirigami inspired self-folding for programming three-dimensional shape shifting of polymer sheets with light. Extreme Mech Lett 2017;11:111–20.
[16] Jaspin S, Anbarasan R, Dharini M, Mahendran R. Morphological analysis of corn xerogel and its shape shifting in water. J Food Eng 2022;330:111107.
[17] Cerda E, Ravi-Chandar K, Mahadevan L. Thin films - Wrinkling of an elastic sheet under tension. Nature 2002;419:579–80.
[18] Nayyar V, Ravi-Chandar K, Huang R. Stretch-induced stress patterns and wrinkles in hyperelastic thin sheets. Int J Solids Struct 2011;48(25):3471–83.
[19] Fu C, Wang T, Xu F, Huo Y, Potier-Ferry M. A modeling and resolution framework for wrinkling in hyperelastic sheets at finite membrane strain. J Mech Phys Solids 2019;124:446–70.
[20] Wang T, Yang Y, Fu C, Liu F, Wang K, Xu F. Wrinkling and smoothing of a soft shell. J Mech Phys Solids 2020;134:103738.
[21] Hu Y, Leng J, Jia F, Liu Y. Peeling behavior of a film on inner surface of a tube. Extreme Mech Lett 2023;58:101930.
[22] Matsuo ES, Tanaka T. Patterns in shrinking gels. Nature 1992;358:482–5.
[23] Fu Y, Jin L, Goriely A. Necking, beading, and bulging in soft elastic cylinders. J Mech Phys Solids 2021;147:104250.
[24] Siéfert E, Cattaud N, Reyssat E, Roman B, Bico J. Stretch-induced bending of soft ribbed strips. Phys Rev Lett 2021;127:168002.
[25] Hu Y, Zeng C, Amar MB, Jia F, Liu Y, Leng J. Thermo-aqueous coupling behaviors for shape memory hydrogels: A statistical–mechanical model and simulations faced with experiments. Int J Solids Struct 2023;112395.
[26] Osada Y, Matsuda A. Shape memory in hydrogels. Nature 1995;376(6537). 219–219.
[27] Hao J, Weiss R. Mechanically tough, thermally activated shape memory hydrogels. ACS Macro Lett 2013;2(1):86–9.
[28] Hu X, Zhang D, Sheiko SS. Cooling-triggered shapeshifting hydrogels with multi-shape memory performance. Adv Mater 2018;30(26):1707461.
[29] Liu K, Zhang Y, Cao H, Liu H, Geng Y, Yuan W, Zhou J, Wu ZL, Shan G, Bao Y, Zhao Q, Xie T, Pan P. Programmable reversible shape transformation of hydrogels based on transient structural anisotropy. Adv Mater 2020;32(28):2001693.
[30] Ni C, Chen D, Yin Y, Wen X, Chen X, Yang C, Chen G, Sun Z, Wen J, Jiao Y, et al. Shape memory polymer with programmable recovery onset. Nature 2023;622(7984):748–53.
[31] Korde JM, Kandasubramanian B. Naturally biomimicked smart shape memory hydrogels for biomedical functions. Chem Eng J 2020;379:122430.
[32] Löwenberg C, Balk M, Wischke C, Behl M, Lendlein A. Shape-memory hydrogels: Evolution of structural principles to enable shape switching of hydrophilic polymer networks. Acc Chem Res 2017;50(4):723–32.
[33] Techawanitchai P, Idota N, Uto K, Ebara M, Aoyagi T. A smart hydrogel-based time bomb triggers drug release mediated by pH-jump reaction. Sci Technol Adv Mater 2012.
[34] Zhang Y, Gao H, Wang H, Xu Z, Chen X, Liu B, Shi Y, Lu Y, Wen L, Li Y, et al. Radiopaque highly stiff and tough shape memory hydrogel microcoils for permanent embolization of arteries. Adv Funct Mater 2018;28(9):1705962.
[35] Shang J, Le X, Zhang J, Chen T, Theato P. Trends in polymeric shape memory hydrogels and hydrogel actuators. Polym Chem 2019;10(9):1036–55.
[36] Tian Y, Xu Z, Qi H, Lu X, Jiang T, Wang L, Zhang G, Xiao R, Wu H. Magnetic-field induced shape memory hydrogels for deformable actuators. Soft Matter 2024;20:5314–23.
[37] Chen Y-N, Peng L, Liu T, Wang Y, Shi S, Wang H. Poly (vinyl alcohol)–tannic acid hydrogels with excellent mechanical properties and shape memory behaviors. ACS Appl Mater Interfaces 2016;8(40):27199–206.
[38] Wang Q, Liu Z, Tang C, Sun H, Zhu L, Liu Z, Li K, Yang J, Qin G, Sun G, et al. Tough interfacial adhesion of bilayer hydrogels with integrated shape memory and elastic properties for controlled shape deformation. ACS Appl Mater Interfaces 2021;13(8):10457–66.
[39] Yin Q, Tu S, Chen M, Wu L. Bioinspired design of reinforced gradient hydrogels with rapid water-triggered shape memory performance. ACS Appl Polym Mater 2020;2(7):2858–66.
[40] Chen J, Huang J, Hu Y. 3D printing of biocompatible shape-memory double network hydrogels. ACS Appl Mater Interfaces 2020;13(11):12726–34.
[41] Shiblee MNI, Ahmed K, Kawakami M, Furukawa H. 4D printing of shape-memory hydrogels for soft-robotic functions. Adv Mater Technol 2019;4(8):1900071.
[42] Wang Z, Gu J, Zhang D, Zhang Y, Chen J. Structurally dynamic gelatin-based hydrogels with self-healing, shape memory, and cytocompatible properties for 4D printing. Biomacromolecules 2022;24(1):109–17.
[43] Tang L, Huang J, Zhang H, Yang T, Mo Z, Qu J. Multi-stimuli responsive hydrogels with shape memory and self-healing properties for information encryption. Eur Polym J 2020;140:110061.
[44] Chen Y, Zhang H, Chen J, Kang G, Hu Y. Hyperelastic model for polyacrylamide-gelatin double network shape-memory hydrogels. Acta Mech Sin 2021;37:748–56.
[45] Xue Y, Zhou Z, Lei J, Liu Z. A constitutive model of water-triggered shape memory hydrogels and its finite element implementation. J Appl Mech 2023;90(7):071005.
[46] Li G, Zhang H, Fortin D, Xia H, Zhao Y. Poly (vinyl alcohol)–poly (ethylene glycol) double-network hydrogel: a general approach to shape memory and self-healing functionalities. Langmuir 2015;31(42):11709–16.
[47] Vernerey FJ, Long R, Brighenti R. A statistically-based continuum theory for polymers with transient networks. J Mech Phys Solids 2017;107:1–20.